H24 火山性流体討論会＆地殻流体シーズナルスクール

岩石組織形成に対する粒間流体の役割

地球深部流体の物理化学的性質：基礎をはじめに復習

“Geological fluids (地質流体)”の種類（主成分）

- 水（液体・気体）
- 超臨界水・超臨界CHO系流体
- 珪酸塩メルト
- 珪酸塩メルトと超臨界水の混和状態
- 炭酸塩メルト（カーボナタイト）
- 硫化物メルト
- （溶融金属）

“Geological fluids” (地質流体)の役割

- 固体に比べて圧倒的に速く物質と熱を運搬する
- 固体と物性が大きく異なる
  （流体を含む岩石は物性が大きく変わる）

⇒ 地球の化学進化
地球のダイナミックス

流体の関与する重要な現象の例

☆ 変成作用・岩石ー水反応
☆ 鉱床形成・鉱化作用
☆ フラックス融解
☆ 部分溶融マントル・地殻からのメルトの分離
☆ マグマ溜まりプロセス
☆ マントルメタソマティズム
☆ 核形成
・・・・・・

流体の存在量・岩石微細構造に強く依存する岩石物性

+ 密度　Density
+ 粘性　Viscosity
+ 浸透率　Permeability
+ 全岩での拡散係数　Bulk diffusivity
+ 弾性波速度（異方性）
+ 電気伝導度

・・・・・・

Regimes in Fluid-bearing Rock Systems

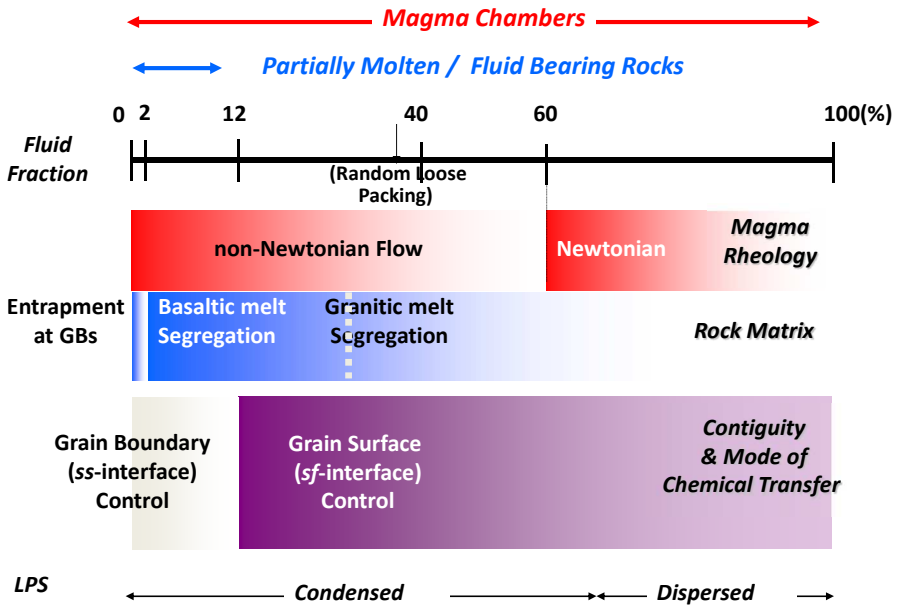

1%の流体とはどれくらいの量？

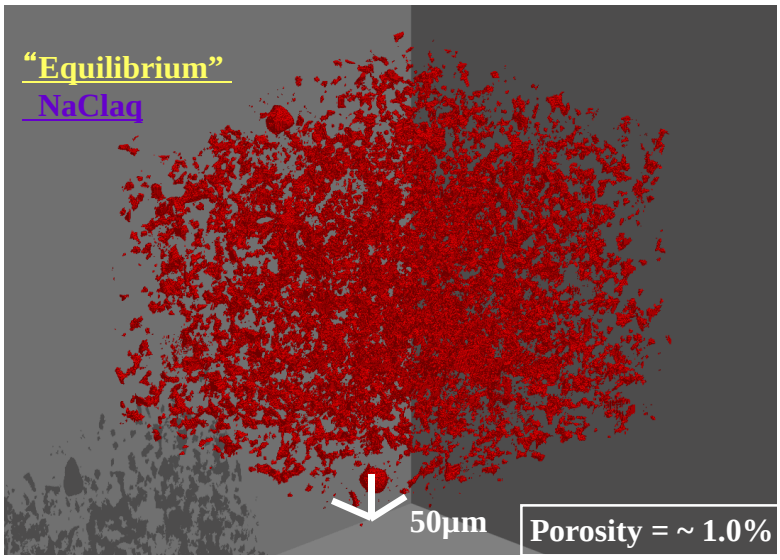

水の三態と臨界点

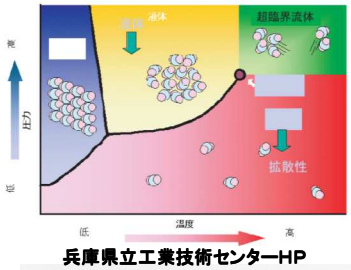

兵庫県立工業技術センターHP

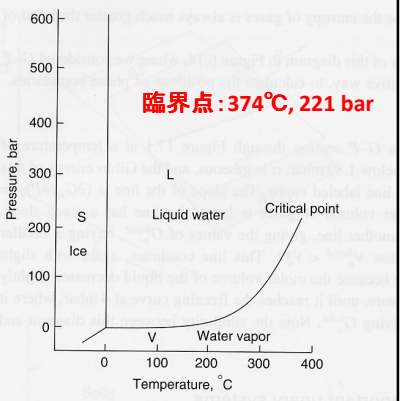

臨界点：374℃, 221 bar

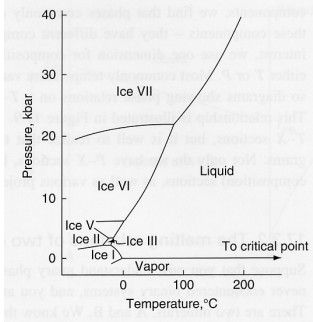

Anderson (2005)
Thermodynamics of Natural system, Cambridge

超臨界流体は、液体の高い分子密度と
気体の大きい分子運動エネルギーを兼ね備える

臨界点と超臨界流体

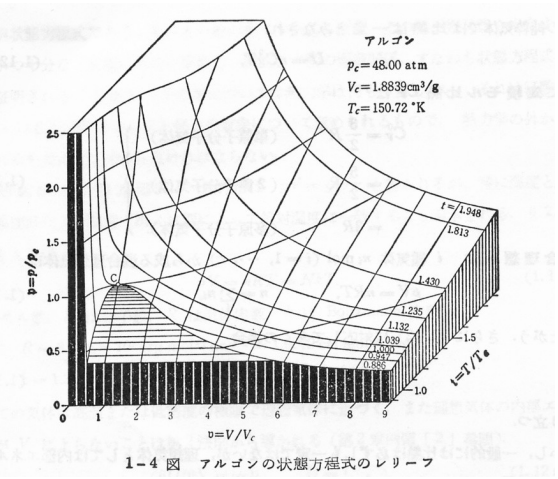

1–4 図　アルゴンの状態方程式のレリーフ

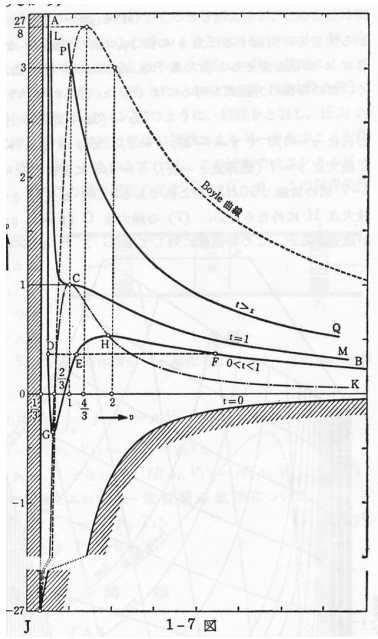

1–7 図

実在気体の状態方程式の例（van der Waalsの式）

$$\left(P+\frac{a}{V^2}\right)(V-b)=RT$$

久保亮吾　熱学統計力学　裳華房

圧縮因子と臨界定数

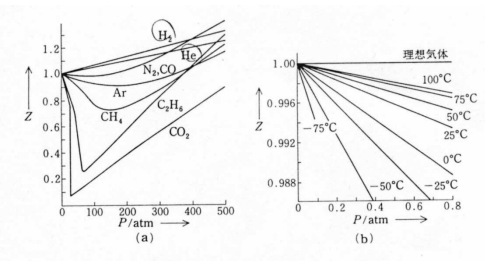

図 1-3 （a） 圧縮率因子の圧力変化（温度はエタン（37°C）以外は0°C）
（b） アンモニアの圧縮率因子の温度依存性

表 1-3　単体および無機化合物の臨界定数（1 atm = 101325 Pa）

化学式	t_C / °C	P_C / atm	ρ_C / g·cm^{-3}	$\frac{P_C V_C}{RT_C}\left(=\frac{P_C M}{RT_C \rho_C}\right)$
Ar	−122.4	48.1	0.533	0.291
Br_2	311	102	1.26	0.288
CO	−140.24	34.53	0.301	0.294
CO_2	31.0	72.8	0.468	0.274
CS_2	279	78	0.44	0.298
Cl_2	144	76	0.573	0.275
D_2	−234.9	16.3	0.0669	0.313
F_2	−128.85	51.47	0.574	0.288
HBr	90.0	84.4	—	—
HCl	51.5	82.0	0.45	0.249
HI	150.8	82	—	—
H_2	−240.17	12.76	0.0314	0.303
H_2O	373.99	217.6	0.32	0.230
H_2S	100.0	88.2	0.346	0.283
He	−267.96	2.24	0.0698	0.303
NH_3	132.4	111.3	0.235	0.242
NO	−93	64	0.52	0.250
NO_2	158	100	0.55	—
N_2	−147.0	33.5	0.313	0.292
Ne	−228.75	27.2	0.484	0.312
O_2	−118.57	49.77	0.436	0.288
O_3	−12.1	55	0.54	0.228
PH_3	51.6	64.5	—	—
SF_6	45.54	37.10	0.736	0.282
SO_2	157.6	77.81	0.525	0.306
Xe	16.583	57.64	1.11	0.290

物理化学の基礎　西川・渡辺　学術図書 1979

超臨界流体の熱力学的性質

Specific volume

$$\left(\frac{\partial G}{\partial P}\right)_T = V$$

$$\int_{P_1}^{P_2} dG = \int_{P_1}^{P_2} V dP$$

V=V(P, T):状態方程式

Entropy

$$\left(\frac{\partial P}{\partial T}\right)_S = \frac{T}{C_P}\left(\frac{\partial V}{\partial T}\right)_P$$

> 0

Figure 6.1 The specific volume ($cm^3\,g^{-1}$) of water as a function of P and T. Dashed contours are water fugacity in bars. Small dot indicates the critical point. Data from the program STEAM (§13.6.1)

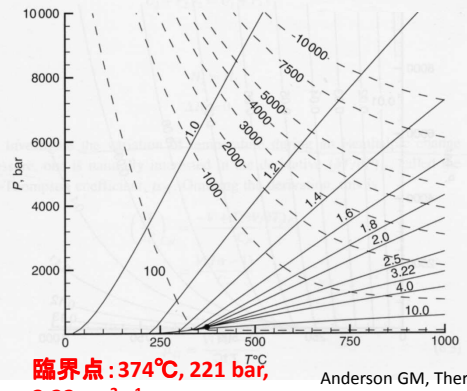

Figure 6.2 The entropy of water in $kJ\,mol^{-1}$ as a function of P and T. Data from the program STEAM of Harvey et al. (2000).

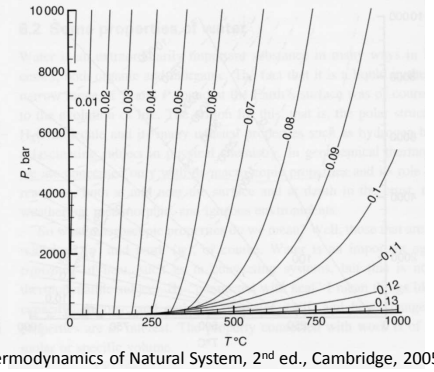

臨界点:374℃, 221 bar, 3.22 cm^3g^{-1}

Anderson GM, Thermodynamics of Natural System, 2nd ed., Cambridge, 2005

C.E. Manning / Earth and Planetary Science Letters 223 (2004) 1–16

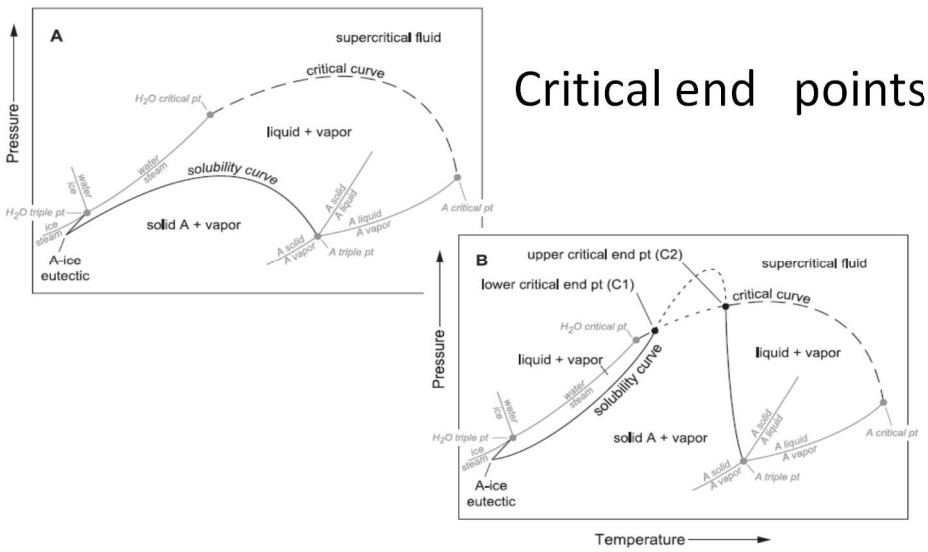

Critical end points

Fig. 3. Schematic $P-T$ projections of phase relations illustrating contrasting behavior of simple two-component systems. Grey lines indicate phase relations for one-component systems H_2O and hypothetical composition A; black lines represent relations for A-H_2O mixtures. Labeling of fields is for H_2O-rich systems. (A) The system A-H_2O, in which the critical curve and solubility curve do not intersect. NaCl–H_2O is an example of such a system. (B) The system A-H_2O, in which the critical curve and solubility curve intersect. This yields two critical end points (C1 and C2). Short dashed lines denote metastable portions of curves. Albite–H_2O is an example.

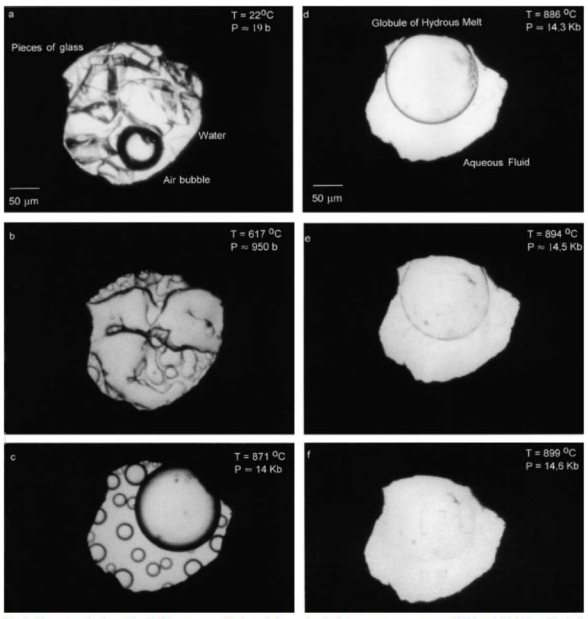

Fig. 1. The system haplogranite–H_2O in an externally heated diamond cell, from room temperature to 899°C and 14.6 kbar. The bulk density of water in this experiment was 0.95 g cm^{-3}. For further explanations see text.

H. Bureau, H. Keppler / Earth and Planetary Science Letters 165 (1999) 187–196

様々なケイ酸塩メルトと
hydrous fluidの混和:
外熱DAC実験

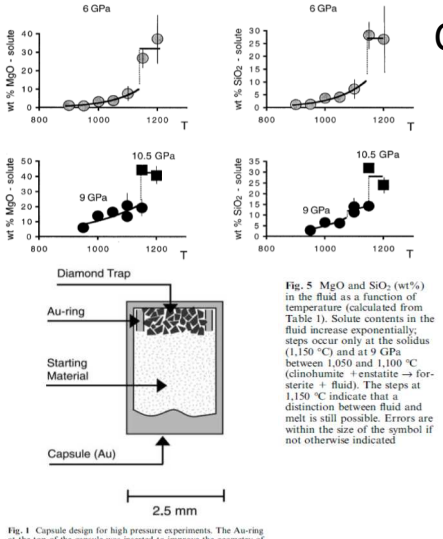

Fig. 5 MgO and SiO_2 (wt%) in the fluid as a function of temperature (calculated from Table 1). Solute contents in the fluid increase exponentially; steps occur only at the solidus (1,150 °C) and at 9 GPa between 1,050 and 1,100 °C (clinohumite + enstatite → forsterite + fluid). The steps at 1,150 °C indicate that a distinction between fluid and melt is still possible. Errors are within the size of the symbol if not otherwise indicated

Fig. 1 Capsule design for high pressure experiments. The Au-ring at the top of the capsule was inserted to improve the geometry of the diamond trap. A less elongated trap facilitates the analyses by laser ablation. The size of the diamonds is not to scale. Diamonds used in an early stage of the study were 50 µm in diameter. Subsequently, the precision of the results could be improved by using smaller diamonds (20 µm in diameter)

MgO-SiO_2-H_2O: 20 GPa, 1150℃
Lhez-CO_2-H_2O: >7.5 GPa, 1000℃
(Wyllie &Ryabchikov, 2000, J. Petrol)

C2 in the mantle system at higher pressures

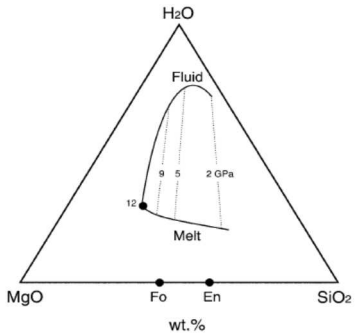

Fig. 9 Fluid and melt compositions (wt%) at the respective solidus temperature for several different pressures (summarised from Fig. 8). Both fluid and melt exhibit an enhanced Mg/Si with increasing pressure. Probably the fluid approaches the composition of the melt at pressures significantly higher than 10 GPa. Note that with increasing pressure the solute content of the fluid changes much more than the water content of the melt

R. Stalder · P. Ulmer · A. B. Thompson · D. Günther

Contrib Mineral Petrol (2001) 140: 607–618
DOI 10.1007/s004100000212

沈み込み帯の流体は
“Second Critical End Point”
を超える場合がある

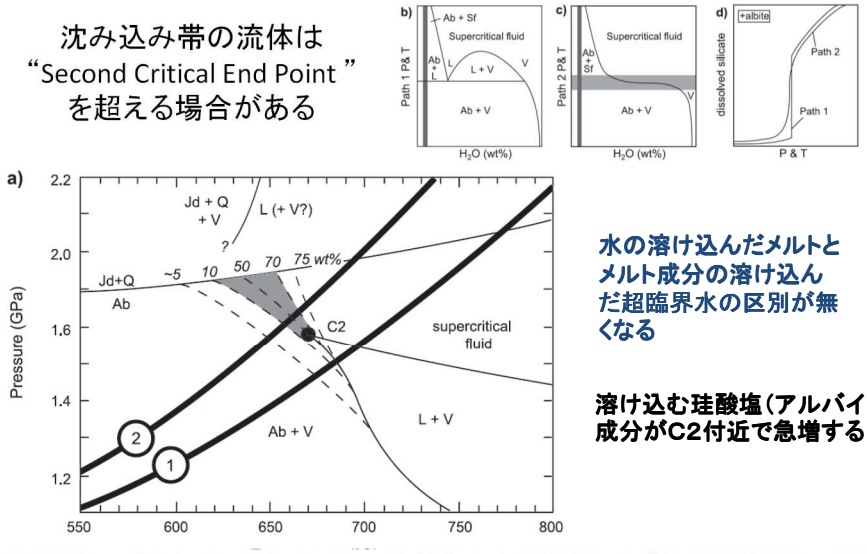

水の溶け込んだメルトとメルト成分の溶け込んだ超臨界水の区別が無くなる

溶け込む珪酸塩（アルバイト）成分がC2付近で急増する

Fig. 4. (a) *PT* diagram illustrating phase relations near the second critical end point (C2) in the system albite–H_2O. Critical curve, solubility curve, and isopleths of albite solubility (dashed, in wt.%) from [71,72]. Thick solid lines represent two schematic subduction paths passing below (1) and above (2) the critical end-point. Shading indicates the region of greatest change in fluid composition. The Jd + Q solidus is queried because it is not known how it is affected by C2. Abbreviations: Ab, albite, Jd, jadeite; L, liquid; Q, quartz; Sf, supercritical fluid; V, vapor. (b) Phase relations of albite–H_2O along Path 1 as function of H_2O concentration. (c) Phase relations of albite–H_2O along Path 2 as a function of H_2O concentration. Light shading represents the region shaded in (a). In (b) and (c), the dark shaded band represents typical H_2O contents of geologic systems. (d) Comparison of the variation in dissolved silicate in the phase coexisting with albite along Paths 1 and 2.

- 1～2GPaでunmixingに
- Amphibole dehydration領域ではimmiscible
- Phengite, lawsoniteの分解はmiscible領域

Critical curveのPT

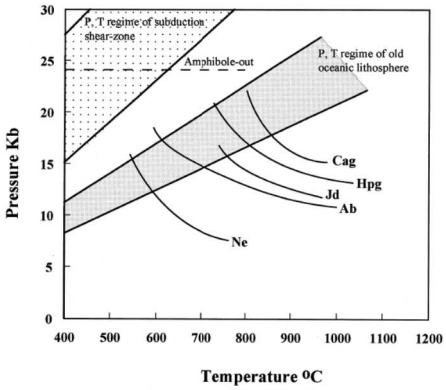

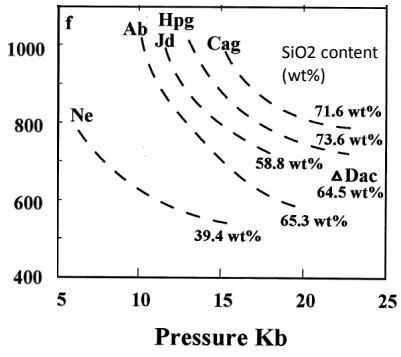

Fig. 5. Location of the critical curves in various silicate melt–H_2O systems relative to the conditions of amphibole dehydration [24], the P.T regime of old oceanic lithosphere [27], and the P.T regime of a subducted slab [28]. *Ne* = nepheline; *Ab* = albite; *Jd* = jadeite; *Hpg* = haplogranite; *Cag* = Ca-bearing granite.

Table 1
Compositions of the starting glasses in wt.%

	Haplogranite	Ca-bearing granite	Dacite	Tholeiite	Nepheline	Jadeite
N[a]:	58	39	49	54	68	46
SiO_2	73.65 ± 0.32	71.60 ± 0.62	64.51 ± 0.26	51.09 ± 0.34	39.42 ± 0.23	58.80 ± 0.28
Al_2O_3	11.77 ± 0.19	13.29 ± 0.15	16.20 ± 0.11	14.78 ± 0.10	30.35 ± 0.19	22.94 ± 0.15
Na_2O	4.66 ± 0.08	3.94 ± 0.10	4.07 ± 0.09	2.86 ± 0.08	14.15 ± 0.15	14.18 ± 0.17
K_2O	4.26 ± 0.06	3.54 ± 0.06	1.17 ± 0.03	0.46 ± 0.02	9.14 ± 0.09	0
CaO	0	1.93 ± 0.04	6.41 ± 0.10	15.08 ± 0.15	0	0
MgO	0	0	3.26 ± 0.05	10.68 ± 0.10	0	0
Total	94.34	94.30	95.62	94.95	93.06	95.92
H_2O[b]	5.02	4.89	3.80	4.62	4.82	3.06
Total (with water)	99.36	99.19	99.42	99.57	97.88	98.58

[a] Number of microprobe analysis. [b] Water contents were determined by Karl Fisher titration (±0.2 wt.%).

haplogranite-H_2O系solvus（ 12.5～16.9 kb）

Supercritical fluidはmeltに比べH2O高くOH低い

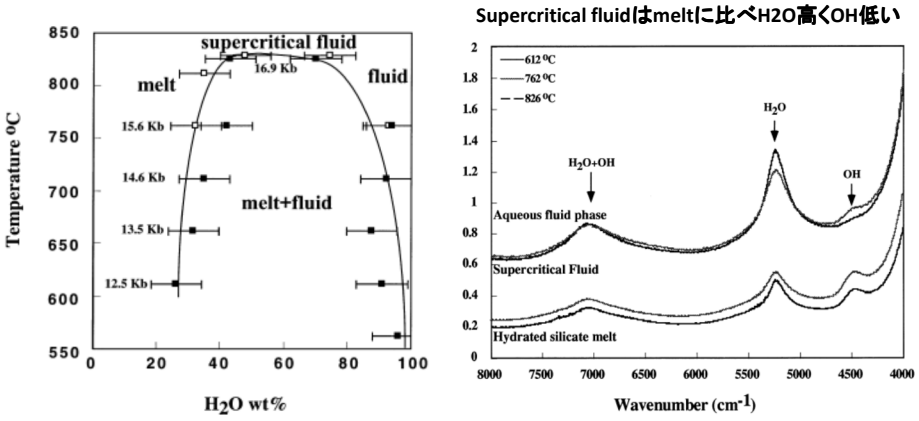

Fig. 4. Phase diagram of the system haplogranite–H_2O under isochoric conditions for a bulk density of water of 1.016 g cm^{-3}. The compositions of the coexisting phases were derived from in-situ FTIR spectra. Open and closed symbols refer to two different sets of measurements.

・Hydrous fluid中のsilicate成分濃度は低い
・solvus頂部がflat

F, B, P の効果: ごく低圧（1kb）で珪酸塩メルトと熱水が完全混和

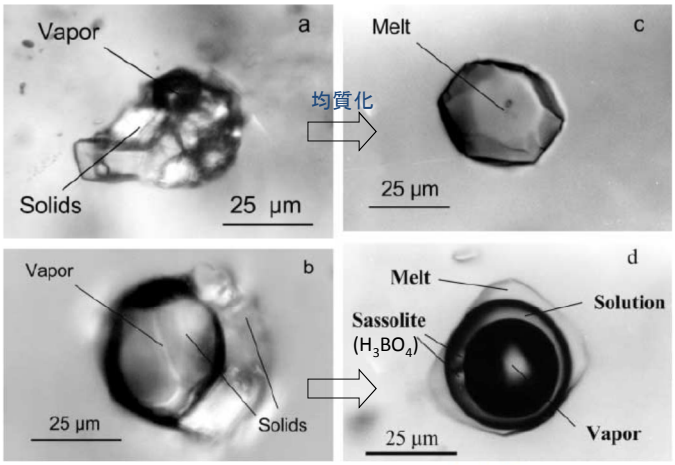

pegmatite中のmelt inclusion

R. Thomas · J. D. Webster · W. Heinrich
Contrib Mineral Petrol (2000) 139: 394–401

Fig. 1 Melt inclusions in pegmatite quartz from Ehrenfriedersdorf, Germany. **a** A-type melt inclusion. Solids (feldspars, quartz, mica, and others) occupy about 80% of the total inclusion volume. **b** B-type melt inclusion. Solids (feldspars, quartz, mica, and others) occupy about 60% of the total inclusion volume. **c** A-type melt inclusion, completely rehomogenized at 650 °C and 1 kbar. **d** B-type melt inclusion, completely rehomogenized at 650 °C and 1 kbar. Phase separation into glass, liquid, and vapor occurred during quenching

1 kbでのsolvus (均質化実験結果)

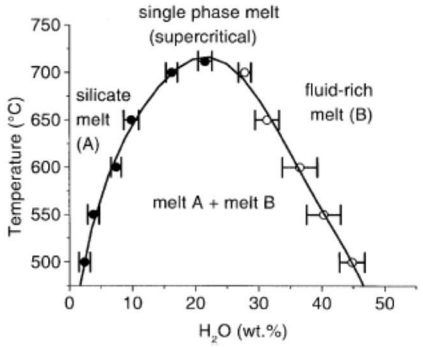

Fig. 3 Pseudobinary wt% H_2O versus temperature plot of rehomogenized A-type (closed circles) and B-type melt inclusions (open circles) in pegmatite quartz Qu8 from Ehrenfriedersdorf, Erzgebirge, Germany. Pressure is ~1 kbar

・ほぼimmiscible “melts”
・solvus頂部が狭い

Table 2 Representative oxide and element concentrations in the A-type and B-type melt inclusions homogenized at 650 °C and 1 bar. *d.l.* Detection limit, *n.d.* not determined

	A-type inclusion	B-type inclusion (glass portion)	B-type inclusion (glass + solution[a])
SiO_2	64.50 ± 1.09	61.08 ± 1.2	37.98[b]
TiO_2	0.02 ± 0.01	d.l.	–
SnO_2	0.10 ± 0.02	0.80 ± 0.06	0.48[b]
Al_2O_3	11.69 ± 0.52	14.04 ± 0.77	8.74[b]
B_2O_3	0.20[c]	n.d.	4.12[d]
FeO	0.29 ± 0.05	2.04	1.27[b]
MnO	0.04 ± 0.01	0.15	0.07[b]
MgO	d.l.	d.l.	–
CaO	0.03 ± 0.01	d.l.	
Na_2O	3.20 ± 0.14	3.33 ± 0.56	2.85
K_2O	3.01 ± 0.55	3.33 ± 0.43	3.37
Rb_2O	0.44 ± 0.04	0.55	> 0.35[b]
Cs_2O	0.12	1.49 ± 0.24	0.92[b]
P_2O_5	3.20 ± 0.31	0.92	0.57[b]
F	4.50 ± 0.25	4.19	2.60[b]
Cl	0.14 ± 0.02	0.35 ± 0.02	5.78
H_2O	9.80 ± 1.2	9.0 ± 0.7[e]	31.80[e]
Sum	101.28	101.27	100.90
ASI	1.32	1.42	0.99

[a] The aqueous phase contains 8.5 ± 1.1 wt% NaCl eq.; NaCl/KCl ~1 (from cryometric measurements)
[b] Calculated assuming presence only in the glass portion
[c] Determined by ion microprobe (SIMS) at Woods Hole Oceanographic Institution, MA, USA, as a maximum (see Webster et al. 1997)
[d] Calculated from the boron acid (H_3BO_3) concentration in the liquid of B-type melt inclusions. According to the melting temperature of 51 ± 1.5 °C of the sassolite daughter crystals, a concentration of 10.5 wt% H_3BO_3 in the liquid was estimated
[e] Value from Table 1

三相不混和流体の例

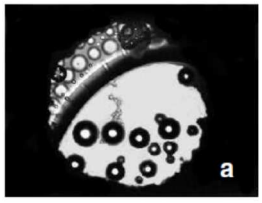

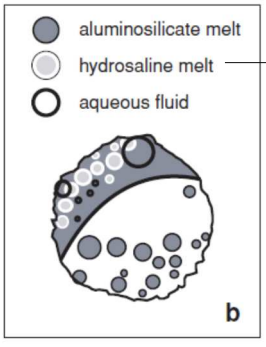

A starting glass with the bulk composition (in wt%): SiO_2 = 58.7, Al_2O_3 = 16.5, B_2O_3 = 5.0, Na_2O = 2.9, K_2O = 3.7 Rb_2O = 1.1, Cs_2O = 1.0, Li_2O = 0.5, P_2O_5 = 4.2, F 4.6, and H_2O = 1.5 was

→contains (in wt%): SiO_2 = 23.2, Al_2O_3 = 21.4, B_2O_3 = 15.6, Na_2O = 5.1, K_2O = 2.4, Rb_2O = 1.1, Cs_2O = 1.0, P_2O_5 = 2.6, F = 17.5, the remaining 18% being mostly H_2O and minor Li_2O.

(550℃, 0.2GPa)

FIGURE 1. Photomicrograph (a) and explanatory sketch (b) of a plan view into the sample chamber of HDAC during slow cooling from 830 to 810 °C and ~0.4 GPa. Globules of hydrosaline melt and fluid bubbles nucleated and grew inside aluminosilicate melt while beads of the aluminosilicate melt precipitated from the hydrous fluid implying close approach to thermodynamic equilibrium. The diameter of the sample chamber is 0.4 mm.

Determination of liquid/vapor partitioning of Cu and Zn by using synthetic fluid inclusion method and SR-XRF

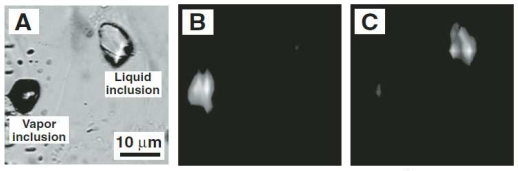

Figure 1. Typical example of Cu and Zn measurement in fluid inclusions synthesized under sulfur-rich conditions (run 18B). A: Optical microscopic image of X-ray irradiated area. Both vapor-rich and liquid-rich inclusions are present. B: Fluorescent X-ray image of Cu showing concentration in the vapor inclusion. C: Fluorescent X-ray image of Zn showing concentration in the liquid inclusion.

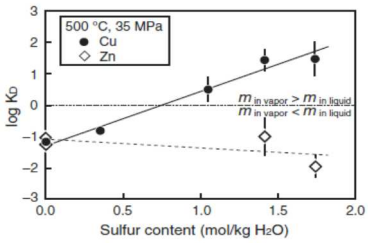

Figure 3. Vapor-liquid distribution constant (log K_D) for Cu and Zn and its dependence on sulfur content at 500 °C and 35 MPa.

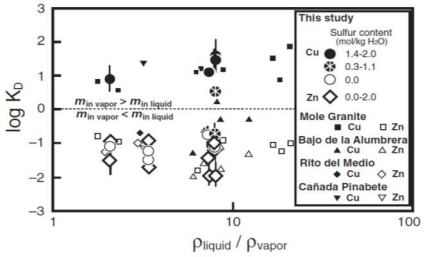

Figure 4. Comparison of log K_D values for Cu and Zn obtained in this study (both S-bearing and S-free experiments) with natural samples. Analytical data for coexisting vapor- and liquid-rich inclusions in hydrothermal ore deposits are from the Mole Granite (Audétat et al., 2000), the Bajo de la Alumbrera (Ulrich et al., 2001), the Rito del Medio pluton (Audétat and Pettke, 2003), and the Cañada Pinabete pluton (Audétat and Pettke, 2003).

Nagaseki H. & Hayashi K.
Geology, January 2008; v. 36; no. 1; p. 27–30; doi: 10.1130/G24173A.1

岩石中での超臨界流体の分布形態と移動様式

粒子スケールでの流体分布・連結度の支配要因:“二面角”と流体量

（理想的で単純な系）

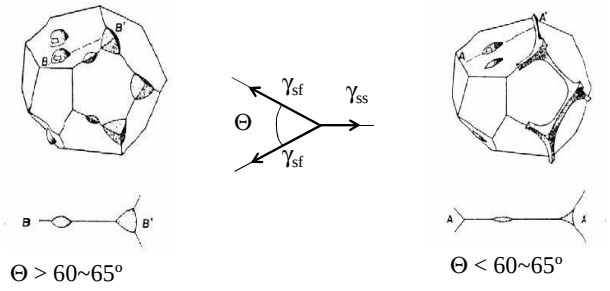

Θ > 60~65°

Θ < 60~65°

流体は少量では連結せず孤立する
→浸透流として流れず、割れ目が必要

流体は少量で連結する
→浸透流になり得る

岩石中における連結した流体（二面角小）の形状

（イメージ）

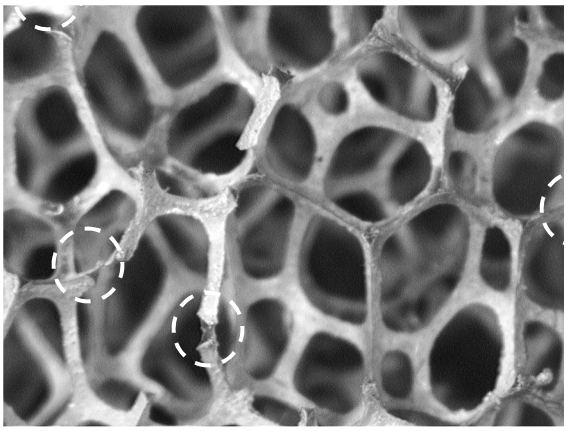

流体の巨視的な移動様式は粒子サイズでの流体の形状に依存する。
←流体の形状は、結晶と流体の濡れ易さ（界面張力のバランス）という物質の性質によって決まる

Fluid geometry calculation

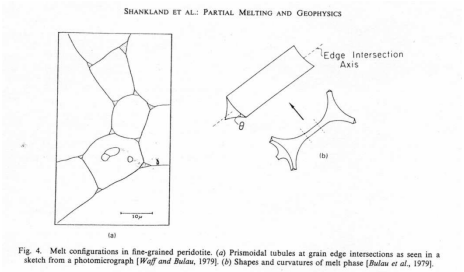

Fig. 4. Melt configurations in fine-grained peridotite. (*a*) Prismoidal tubules at grain edge intersections as seen in a sketch from a photomicrograph [*Waff and Bulau*, 1979]. (*b*) Shapes and curvatures of melt phase [*Bulau et al.*, 1979].

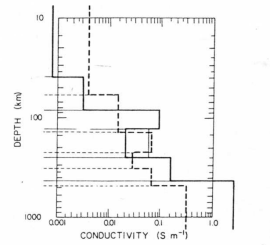

Fig. 3. Oceanic electrical conductivity profiles with high conductivities at depths associated with the seismic low-velocity zone [*Filloux*, 1980].

Shankland et al.,1981, JGR, 19, 394

F = 1%

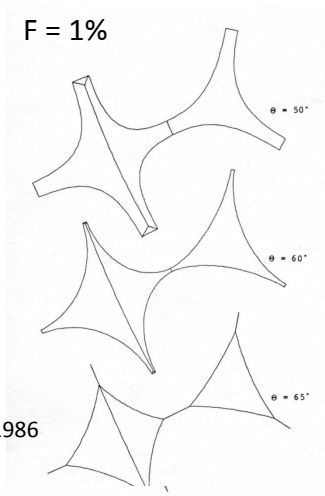

Von Bargen & Waff 1986
JGR, 91, 9261

Fig. 6. Melt channel shapes at a constant melt fraction f=1.0% and wetting angles between 50° and 65°. The change in shape between 20° and 50° (see Figure 5) is minor, compared to the change close to 60°.

Equilibrium Microstructure ("textural equilibrium")

"組織平衡"

溶解ー沈殿作用による
界面エネルギーの
局所的な極小化

↑範囲は曖昧

必要な物質輸送の距離:

個々のporeの組織平衡
～poreサイズ
＜＜実験産物全体の組織平衡
～実験産物のサイズ

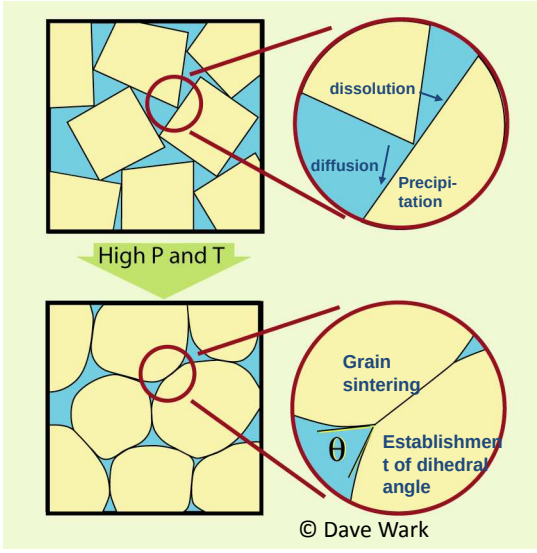

表面（界面）張力

二つの相の境界面の面積を変えるためには仕事が必要になる。
→ **表面張力**に対する仕事
これを含めると、準静的過程に対するエネルギー変化は

$$dU = TdS - p'dV' - p''dV'' + \gamma d\sigma + \mu' dN' + \mu'' dN''$$

p', p''	: 相1，2内部の圧力
$\mu'(T, p'), \mu''(T, p'')$	: 各相の化学ポテンシャル
σ	: 境界面の面積
N', N''	: 相1，2内部の分子数

$$\gamma \equiv \left(\frac{\partial U}{\partial \sigma} \right)_{S,V',V'',N'N''}$$

表面張力に起因する圧力差

相1が半径 r の球であるとき

$$p' - p'' = \frac{2\gamma}{r}$$ Laplaceの式

$dS = dN' = dN'' = 0$ (断熱，物質の生成消滅なし)
$dV'' = -dV'$, $dV'/d\sigma = r/2$ という変形を考え，
平衡条件 $dU = 0$ から導かれる。

例） 半径 r の液滴と蒸気圧 p_r との関係は

$$\mu_l (T, p_r + \frac{2\gamma}{r}) = \mu_g (T, p_r)$$

Over what P-T conditions
can geometric adjustment occur?

1. > Lowest metamorphic grade
(200-300 ºC)
← Existence of fluid inclusions
(Fracture healing,
Grain boundary migration)

2. Healing Rate of Fracture & Cracks
> Plastic Deformation Rate
(Watson & Brenan, 1987, EPSL)

3. Fluid production rate < Dispersion rate
Segregation rate

Scaling Problems

e.g. Partially Molten Peridotite

Time Scale:
Equilibrium pore geometry is maintained at all times
Basalt in dunite (e.g., McKenzie, 1984)
a = 10μm < 200Hr (Vaughan & Kohlstedt, 1982)
a = 1mm < 10^3 yrs << Compaction time scale

Length Scale:
Basalt Infiltration into Dunie (1290ºC) : 0.04-0.08 mm/hr
W = 100m basalt sill may disperse in 200 yr (Watson 1982 Geology)

Cf. Aq. fluid into quartzite (823℃): 0.072±0.018 mm/hr
(Nakamura & Watson 2001 Geofluids)
Carbonatite melt infiltration into dunite: D＝1.8x10^{-9} m^2/s
hundreds thousands of meters / 0.1 - 1 m.y.
(Hammouda & Laporte 2000 Geology)

岩石に保存されているfossil pore fluid geometry 1

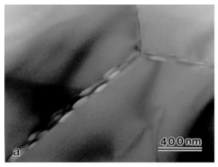

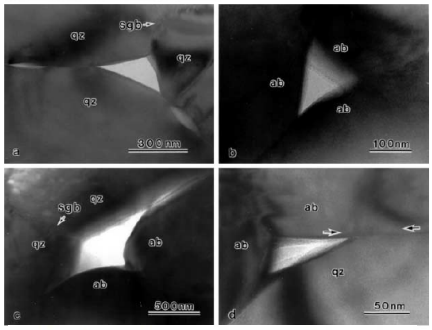

Fig. 2 TEM images of grain-edge pores in the calcite-free sample. **a** Pore at a junction of quartz grains with a sub-grain boundary (*sgb*). **b** Pore at a junction of albite grains. **c** Pore at the junction of quartz and albite grains. **d** Pore at a junction of quartz and albite grains. At the region indicated by *arrows*, the plane of a quartz/albite boundary and pore/albite surface are on a straight line. **e** Pore at a junction of quartz grains with a sub-grain boundary formed by periodic array of dislocations

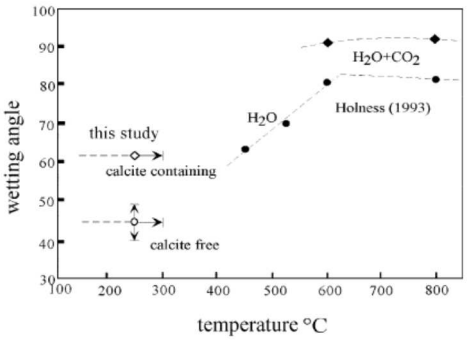

Fig. 8 Plot of wetting angle (quartz–fluid) variation with temperature at 400 MPa from Holness (1993) and comparing angles obtained in this study. The angles measured in this study are plotted at estimated ranges of temperature. *Solid lateral lines* correspond to ranges of peak metamorphic condition and *dotted lines* indicate the possible condition of formation of the wetting angles in the samples. Since there is some deviation between the peak and the median of our wetting angles, a range of values is indicated

Hiraga et al.

Contrib Mineral Petrol (2001) 141: 613–622

岩石に保存されているfossil pore fluid geometry 2

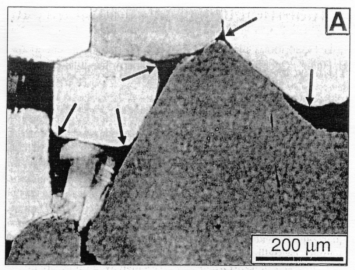

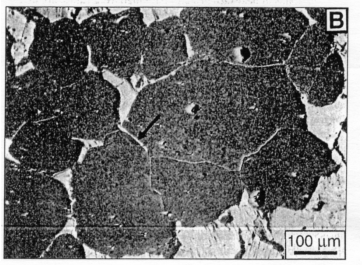

Figure 3. A: Micrograph of sample 9403 (location in Fig. 1) showing quartz grains with interstitial feldspar. Black arrows point to interstitial feldspar at quartz triple-grain junctions. B: Backscattered electron image of sample 9403 showing interstitial feldspar (light gray) at quartz (dark gray) triple junctions. Note curved phase boundaries between quartz and feldspar. Black arrow points to grain boundary entirely coated by feldspar.

Rosenberg & Riller (2000) Geology, 28, 7-10

Figure 4. Cumulative frequency curve of measured apparent dihedral angles. Median value (27°) represents true dihedral angle (see Riegger and van Vlack, 1960, for discussion of this statistical approach).

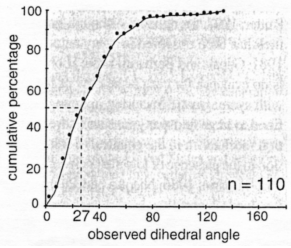

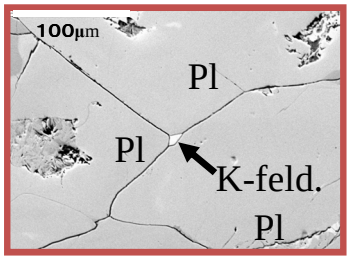

阿武隈花崗岩　宮本複合岩体
（長谷部　2002 東北大修論）

急冷実験産物のpore fluid形状

Quartzite　　Dunite

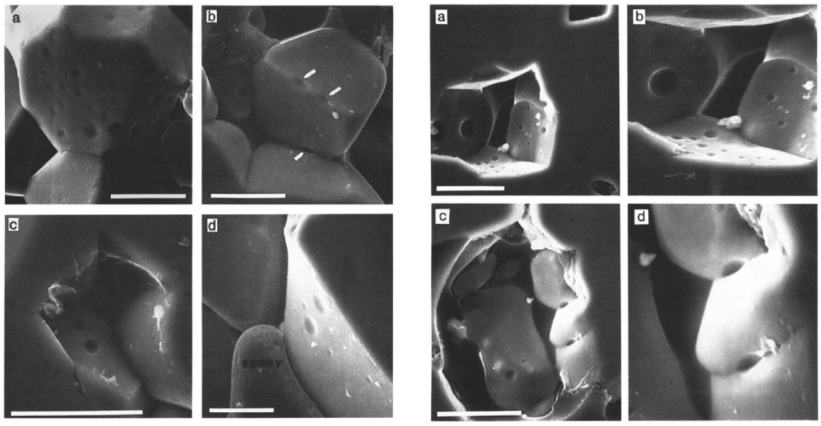

Fig. 5. Selected secondary-electron photomicrographs of regions in synthetic quartzites where grains have been plucked to reveal porosity features in three dimensions. Photo (a) is of run 3 (pure H_2O, $\theta = 57°$); note the numerous surface dimples representing "casts" of once fluid-filled lozenges at grain boundaries. Note also the rounded nature of the grain edges, which formed the walls of fluid channels at run conditions (cf. Fig. 1). Photo (b) is of run 2 ($X_{CO_2} \sim 0.5$, $\theta = 70°$); note the grain-edge "footballs" indicated by the arrows, and compare with the right-hand drawing in Fig. 1c. Photo (c), also of run 2, shows well-defined, apparently deeper dimples than those represented in (a), reflecting the higher wetting angle. The contrast in dimple form is most apparent in a comparison of (c) with (d), which was taken on quartz grains in run 15, in which $\theta \sim 40°$. Note that all photos include some of the epoxy used to impregnate the samples. The white scale bars are 10 μm long.

Watson & Brenan, 1987, EPSL

主な二面角（地殻～最上部マントル）

- メルト：ほぼ60°以下
- 水：60°近傍～60°以上（但し塩濃度の影響大）

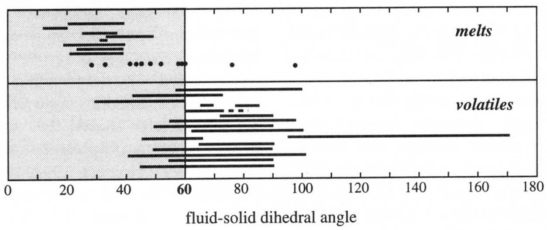

Figure 9.7 Experimentally determined fluid–solid dihedral angles in geological systems. Data are taken from Tables 9.2 and 9.3. Dots represent single reported values, lines show the ranges observed in systems as a function of pressure, temperature and fluid compositional variation. All melt data are ⩽60° apart from 2 isolated pyroxene values (Toramaru and Fujii, 1986) which were later shown to be too high (Fujii, Osamura and Takahashi, 1986; von Bargen and Waff, 1988). All volatile angles occupy a tight group between about 40° and 100° apart from one study (Hay and Evans, 1988) with angles ranging from 97° to 171°. They probably used an inappropriate measuring technique on poorly equilibrated samples (Holness and Graham, 1995). The only study with volatile angles almost exclusively < 60° was Lee, Mackwell and Brantley (1991) and their experiments were probably not fully texturally equilibrated (Brantley, 1992).

Holness（1997）*In*: Jamtveit B. & Yardley, B., Fluid flow and transport in rocks: Mechanisms and Effects, Chapman & Hall, 1977

Effect of fluid chemistry

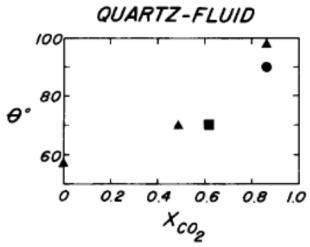

Fig. 3. Wetting angle (θ) vs. CO_2 mole fraction for "CO_2-H_2O" fluids in equilibrium with quartz. Strictly speaking, the fluids are not binary mixtures, but contain some CO at the oxygen fugacity intrinsic to our piston-cylinder assemblies (just below FMQ). The X_{CO_2} values are based on the calculations of Holloway and Reese [21]. Triangles: 950 °; squares: 1000 °; circles: 1150 ° C. See text and Fig. 2.

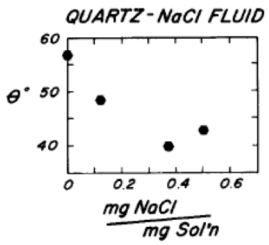

Fig. 12. Wetting angle (θ) vs. NaCl concentration in aqueous fluids in equilibrium with quartz at 1000 ° C and 1 GPa.

Earth and Planetary Science Letters, 85 (1987) 497–515

Fluids in the lithosphere, 1. Experimentally-determined wetting characteristics of CO_2-H_2O fluids and their implications for fluid transport, host-rock physical properties, and fluid inclusion formation

E. Bruce Watson and James M. Brenan

Dihedral angles in the upper mantle 1

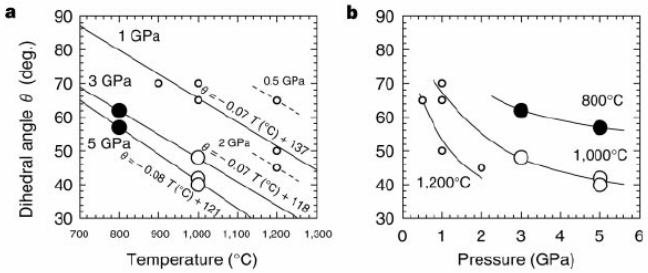

Figure 3 The aqueous fluid–forsterite–forsterite dihedral angle as a function of temperature and pressure. **a**, Temperature; **b**, pressure. The solid lines in **b** do not represent a fit to the data but are merely intended as a guide to the eye. The 800 °C and 1,200 °C curves in **b** are drawn to be consistent with the shape of the 1,000 °C curve. Large solid circle: this study. Large open circle: data from ref. 11. Small open circle: data from ref. 10.

Mibe et al., Nature, 1999

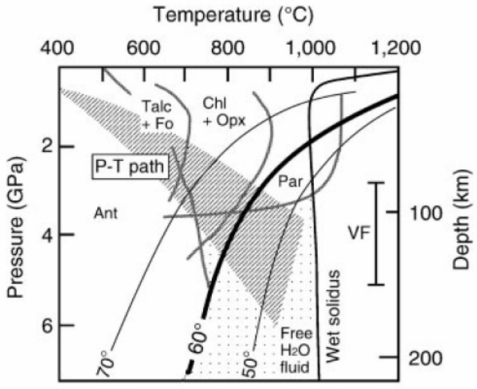

Figure 4 The 60° isopleth of the dihedral angle in aqueous fluid–forsterite–forsterite in *P–T* space. The phase relation in the system peridotite–H_2O[24] is also shown. The downdragged hydrous peridotite (DHP) would be formed at the base of the mantle wedge by the H_2O supplied from the oceanic crust[3–8]. The mechanisms of this migration of H_2O from the oceanic crust to the slab/mantle interface has not yet been clarified, but possible mechanisms include: (1) dihedral angle may also become <60° at higher pressure for minerals which constitute the oceanic crust, although water is non-wetting against those minerals at low pressure[30]; (2) fluid migrates by hydrofracturing[31]; or (3) fluid rises as a diapir within the oceanic crust as a result of inherent buoyancy. The possible *P–T* path[20,21] of the upper surface of DHP is within the shaded region denoted *P–T* path. The thickness of DHP is set to be 3 km as an example. Note that the *P–T* path of the upper surface of DHP intersects the isopleth at depths corresponding to the top of the deep seismic zone (Wadati–Benioff zone) just beneath the volcanic front (range bar denoted VF). The uncertainty in the point at which the 60° isopleth intersects the *P–T* path of DHP is ± 0.5 GPa, which corresponds to a ±2 km in the DHP thickness. Because olivine is anisotropic and the actual mantle is a polyphase mixture rather than pure olivine, an uncertainty of ~±10° in the 60° isopleth is estimated. The shift of the intersections by these effects is indicated by the 50° and 70° isopleths. Abbreviations: Fo, forsterite; Opx, orthopyroxene; Par, pargasite; Chl, chlorite; Ant, antigorite.

Dihedral angles in upper mantle 2

S. Ono et al. / Earth and Planetary Science Letters 203 (2002) 895–903

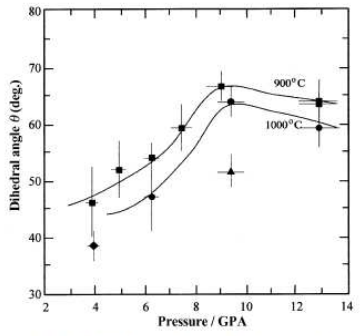

Fig. 3. Dihedral angle versus pressure diagram. The plotted value of the dihedral angle is the median angle. Squares, 900°C; circles, 1000°C; triangle, 1100°C; diamond, 1200°C. The contours are schematic.

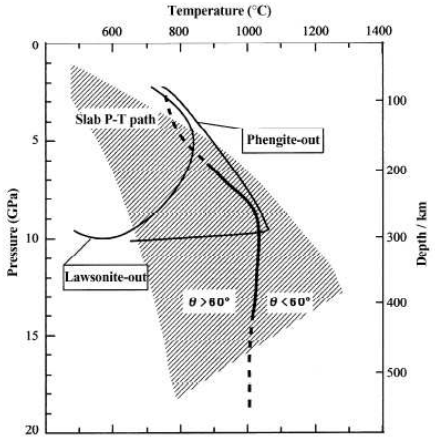

Fig. 4. 60° isopleth of the dihedral angle in fluid–pyrope–pyrope in *P–T* space. The limit of lawsonite and phengite breakdown in the system MORB–H_2O [11,15] is also shown. The possible *P–T* path of the upper part of the subducted oceanic crust is shown as the shaded region.

Requirements to Minimize Total Interfacial Energy

- Dihedral angle
- Equilibrium fluid fraction
- Uniform mean curvature
- Minimum interfacial area

⇒ Texture Rearrangements

- GB grooving
- Fluid infiltration / Expulsion
- Grain size effect
- Grain growth / Ostwald ripening

Minimum Energy Fluid Fraction

(MEMF, equilibrium melt fraction)

二面角が小さい＝固液界面エネルギーが小さい
＝結晶粒界に流体が浸透すると系のエネルギーが下がる

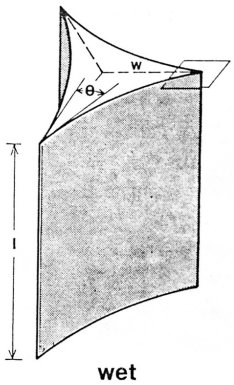

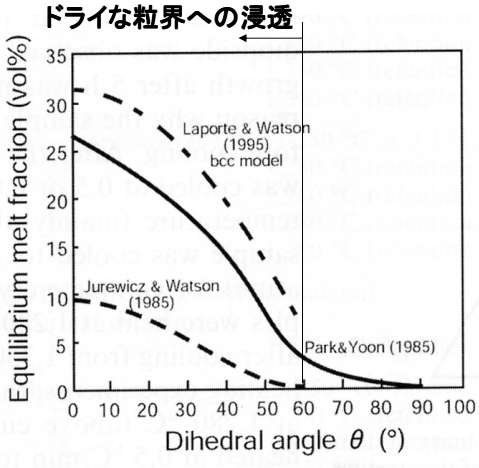

“Grain Size Effect” on the Equilibrium Porosity

Large Curvature **Small Curvature**

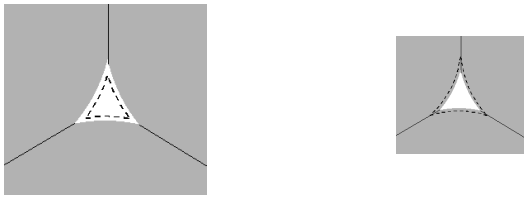

flux

Precipitation ⇐ **Solution**

$$\mu_{coarse} < \mu_{fine}$$

Wark & Watson, 1999

流体量分布の粒径による効果

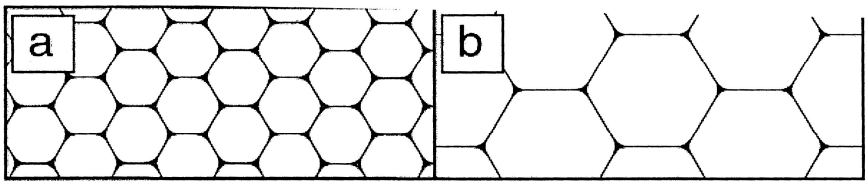

- θ（二面角）、κ（界面曲率）が同じならば必然的に粒子の大きさに因らずporeの大きさは同じになる。

  →細粒領域の方がporeの数が多くなるので、流体量も細粒領域のほうが多くなる。

岩石中の流体移動様式

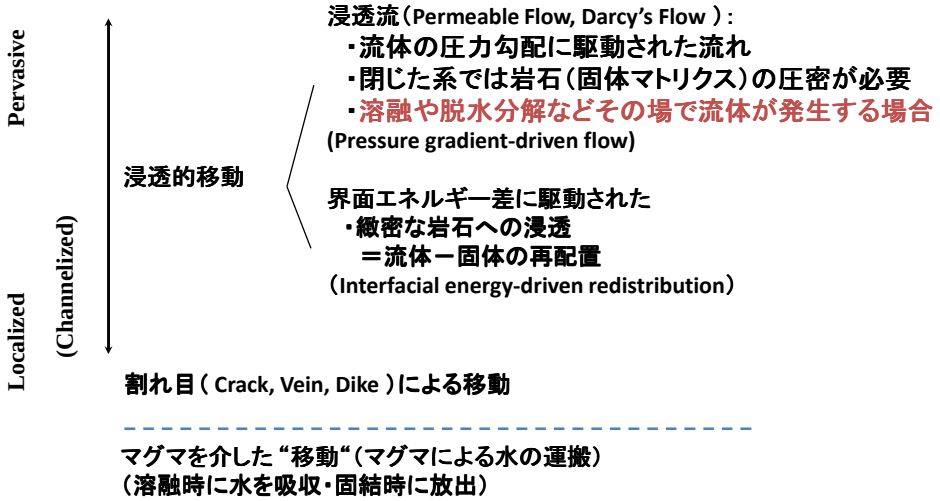

固液共存系における物質輸送の素過程

流体力学的流れ（flow）
>> 流体ネットワーク中の拡散
>> 粒界拡散（grain boundary diffusion）
>> 鉱物内の拡散（lattice diffusion）

ダルシーの法則

流束 ∝ 流体の圧力勾配

$$Q = \frac{\boldsymbol{k}}{\eta} \frac{\Delta p}{d}$$

k: 浸透係数 Permeability

η: 流体の粘度

Large scale fluid migration

…should be rate-limited by
permeability, fluid viscosity, pressure gradient
deformation rate of solid matrix
(interfacial energy-driven fluid redistribution is not effective for km-scale fluid migration)

If so,
What is the principal effect of surface energy?
= Controlling melt interconnectivity and permeability

Indirect, but major influence on the large scale fluid motions (e.g., Waff, 1980, McKezie, 1984, Stevenson, 1986)

Theory (Geometric Adjustment)

- **Pressure difference across a curved surface**

(Kingery et al., 1975)

$$\Delta P = \gamma\left(\frac{1}{r_1}+\frac{1}{r_2}\right)$$

r_1, r_2 : principal radii of curvature

- **Solubility increase due to an applied pressure**

(Thomson-Freundlich equation)

$$\ln\frac{X\kappa}{X_0\kappa_0} = \frac{M\gamma}{\rho RT}\frac{1}{r}$$

Solubility, Activity coeff. over

X, κ: curved surface
X_0, κ_0: flat surface

M: molecular weight
γ: interfacial energy
ρ: density
r: radii of curvature

Theory (Grooving Kinetics)

2-D Grain Boundary

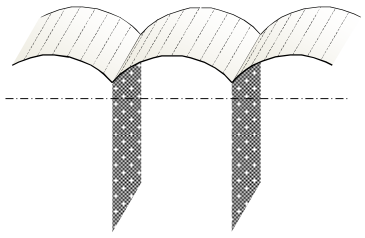

Triple Junction

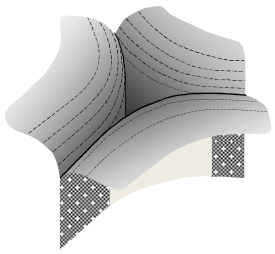

$$d = 1.13\frac{1}{\tan\Theta/2}(At)^{\frac{1}{2}}$$

Dissolution-Precipitation Control

$$d = 0.937\frac{1}{\tan\Theta/2}(Bt)^{\frac{1}{4}}$$

Surface Diffusion Control

(Mullins, 1957)

Geofluids (2001) 1, 73–89

Experimental study of aqueous fluid infiltration into quartzite: implications for the kinetics of fluid redistribution and grain growth driven by interfacial energy reduction

M. NAKAMURA[1] AND E. B. WATSON[2]

[1]Department of Earth and Planetary Sciences, Tokyo Institute of Technology, Tokyo, Japan; [2]Department of Earth and Environmental Sciences, Rensselaer Polytechnic Institute, Troy, New York, USA